Impact of air entrapment on capillary absorption in porous building materials

Fukui, Kazuma

Takada, Satoru

(Citation)
Journal of Building Physics,48(3):318-339

(Issue Date)
2024-11

(Resource Type)
journal article

(Version)
Accepted Manuscript

Title

Impact of air entrapment on capillary absorption in porous building materials

Authors

Kazuma Fukui[1,] *, Satoru Takada[1]

[1]Kobe university, Graduate School of Engineering, 1-1, Rokkodai-cho, Nada-ku, Kobe 657-8501, Japan

*Coresponding author

Email Address: fukui@peridot.kobe-u.ac.jp

Phone No: +81-78-803-6060

1. Introduction

To evaluate the hygrothermal performance of building envelopes with a liquid water supply, such as rain, condensation, and groundwater, it is important to understand the water transfer characteristics of porous building materials with high water content. Particularly, the risks of moisture-related problems, such as frost damage and salt weathering, are highly dependent on the water content in high-water-content regions (Fagerlund, 1977; Feng, et al., 2019) or on the evaporation rates from materials (Rirsch & Zhang, 2010).

Liquid-water transfer and accumulation in porous building materials is not a single-phase phenomenon, as it is affected by the air present in the pore space (Hall, 1977). Porous building materials reach capillary saturation rather than complete saturation after free water absorption (Künzel, 1995). This is most likely because the air remaining in the pores prevents complete water absorption, and after the material reaches capillary saturation, the diffusion and dissolution of air in the pore space are attributed to changes in the water content of the material (Janssen, et al., 2015; Fagerlund, 1994).

Such influences of air have been mentioned in the literature regarding material property measurements. Vacuum saturation tests are commonly conducted to determine the open porosity of a material with pore air rapidly evacuated by a vacuum (Roels, et al., 2004; Feng, et al., 2020). Further, during one-dimensional water absorption tests, small holes are often made on the covering material on the opposite side of the water absorption surface to allow air evacuation while preventing vapor evaporation (Feng, et al., 2015; Feng, et al., 2020). Furthermore, the effects of air pressure on the moisture transfer and retention properties were examined from the viewpoint of the altitude at which the measurements were conducted (Zhou, et al., 2022).

Among these, Janssen et al. (2015) conducted water absorption tests at a reduced air pressure. Their results indicated that water absorption at reduced pressure increased significantly compared to that under atmospheric pressure. Their study provides strong evidence that the influence of air on water transfer in a material cannot be ignored in a high-water-content region, although the data were limited in terms of the employed materials and time evolution.

The air entrapment effects have also been discussed regarding the sealing or surface coating of materials as they can prevent air movement through the surfaces. Descamps (1997) and Fukui et al. (2018) examined the moisture profiles in a sealed material and showed that water transfer is significantly reduced owing to the rising air pressure when sealing the material prevents air from escaping through most of the surfaces. The air pressure increase owing to the low air permeability of the surface sealing is also considered to influence the results of the water absorption tests and cause inter-laboratory errors (Roels, et al., 2004). Iba and Hokoi (2009) demonstrated that the surface coating of roof tiles entrapped air in the specimen during the measurement of water permeability, which could be underestimated.

Many studies have examined the two-phase flow of air and water in soil physics through experiments and numerical simulations (Vachaud, et al., 1974; Green, et al., 1970; Wang, et al., 1998). However, detailed investigations into porous building materials have only been performed under the aforementioned limited conditions, that is, when a material is sealed, except on the water-absorbing surface, or when the material has a low-permeability surface finish.

Therefore, to understand the effects of air entrapment on water transfer in high-water-saturation regions under common water uptake conditions, we further examined the water transfer characteristics corresponding to extremely small air entrapment effects. First, water absorption tests were conducted using several porous building materials, such as bricks, autoclaved aerated concrete (AAC), and calcium silicate board (CS), at reduced air pressures in a vacuum desiccator to compare the time evolution of water absorption with significantly small air entrapment effects with those at atmospheric pressure. Additionally, the water content profiles were compared at atmospheric and low air pressures using the gamma-ray attenuation method. Finally, simultaneous water and air transfer calculations were conducted to confirm the effects of air entrapment on water uptake.

2. Experimental investigation of the water-uptake characteristics at extremely low air pressure

2.1. Methods

2.1.1. Water absorption of three building materials

Figure 1 shows a comparison of the pore volume distributions of the three types of materials employed in this study: bricks, AAC, and CS. The bottom surfaces of the specimens were 40–50 × 60 mm. The height was 100 mm for the brick and CS specimens and 50 mm for AAC, considering the slow absorption of the latter. The sides of the specimens were sealed with modified silicone adhesive and aluminum foil. Most of the tests were conducted under ordinary conditions, except for the surrounding air pressure. The top surface of the specimens was not sealed to ensure no air entrapment on the top surface. All specimens were air-dried before testing.

[insert Figure 1]

For the brick and CS materials, two specimens were prepared: one for testing at atmospheric pressure and one for testing at reduced air pressure. Before the tests, it was confirmed that the absorption rates of the two specimens were similar at atmospheric pressure. In tests using AAC, which has relatively low absorption rates, multiple specimens were used for both atmospheric and low-air-pressure conditions to confirm the differences among specimens. Three specimens were prepared for testing at atmospheric pressure, while four specimens were prepared for testing at reduced air pressure.

The tests were conducted in a laboratory where the temperature was controlled at 23 °C using an air conditioner. The first series of tests was conducted at atmospheric pressure, and the second series

was conducted in a desiccator, in which the air pressure was reduced using a vacuum pump. Considering that the humidity in the desiccator could be higher than that of the air in the laboratory because of evaporation from the water reservoir and the high airtightness of the desiccator, the humidity conditions and water absorption in the desiccator at atmospheric pressure were assessed before the tests. It was confirmed that the humidity in the desiccator was in the hygroscopic region and did not significantly influence water absorption for at least several hours (see Appendix A). The pump speed was 7 L/min and the air pressure in the desiccator was maintained at 2–4 kPa. We avoided using lower pressures to prevent the water from boiling in the reservoir. After the air pressure in the desiccator was reduced, water uptake tests were performed by pouring water into the reservoir.

Water was absorbed from the bottom surfaces of the specimens, whereas the top surfaces were exposed to air in the laboratory or desiccator. During the tests at atmospheric pressure, water uptake was intermittently measured several times to weigh the specimens. Weighting was done within 30 s. During the tests at low pressure, the specimens were weighed only once for each test to prevent them from being exposed to atmospheric pressure during water absorption.

The experimental procedure involved the following steps. First, an air-dried specimen was placed in the desiccator and the pressure inside the desiccator was reduced using a pump. Next, water was poured into a reservoir in the desiccator until the water came into contact with the bottom of the specimen. After a certain period of time from the start of the water uptake, the pressure in the desiccator was restored to the atmospheric pressure, and the specimen was removed from the desiccator and weighted to obtain the water content. Then, the brick and CS specimens were oven-dried for preparation for the next test. For the AAC specimens, this step was skipped as multiple samples were prepared for the tests. Finally, the tests were repeated from an air-dry state, and the water content at different elapsed times was determined to examine the water absorption evolution.

2.1.2. Water content profile during water uptake

To obtain more detailed information on the effects of air entrapment on water uptake, water content distribution measurements were conducted at extremely low air pressures using a gamma-ray attenuation method. The same bricks were used as described in the previous section. The specimen dimensions, sealing conditions, and initial conditions were also the same. Two specimens were prepared: one was used for the experiment at low air pressure and the other was used at atmospheric pressure for comparison.

Figure 2 shows a schematic of the experimental setup. In this study, we used the same gamma-ray apparatus as that used in a previous study (Fukui, et al., 2018; Iba, et al., 2023). The air-dried specimens were placed in a vacuum desiccator between the gamma-ray radiator and detector. The radiator and detector could be moved simultaneously in the vertical direction and the water content profile in the height direction of the specimens was obtained at 10-mm intervals. The data were

acquired approximately every 10 min at each measurement point. The gamma-ray measurements at atmospheric pressure were continued for 1.5 h because of equipment restrictions.

[insert Figure 2]

After passing through the specimen and desiccator, the gamma-ray intensity N (cps) can be expressed as follows (Nielsen, 1972):

$$N = N_0 \exp\left[-\left(\theta_m \rho_m d_m + \mu_l w_l d_m + \theta_b \rho_b d_b + \theta_d \rho_d d_d\right)\right], \quad (1)$$

where N_0 is the gamma-ray intensity at the radiator (cps), d is the thickness (m), θ is the mass attenuation coefficient of the gamma rays for liquid water (m^2/kg), w is the water content (kg/m^3), and ρ is the density (kg/m^3). The subscripts b, d, l, and m represent the moisture barrier (epoxy resin and aluminum foil), desiccator (acrylic), liquid water, and material in the dry state, respectively. Similarly, the gamma-ray intensity N_{int} (cps) at the start of the experiment can be expressed as

$$N_{int} = N_0 \exp\left[-\left(\theta_m \rho_m d_m + \mu_l w_{int} d_m + \theta_b \rho_b d_b + \theta_d \rho_d d_d\right)\right], \quad (2)$$

where w_{nt} is the initial water content of the specimen (kg/m^3). From Equations (1) and (2), the change in water content from the initial state is expressed as

$$w_l - w_{int} = -\frac{1}{\mu_l d_m} \ln\left(\frac{N}{N_0}\right). \quad (3)$$

In this experiment, w_{int} was considered to be zero because the water content of the bricks in the air-dried state was significantly low.

2.2. Results

2.2.1. Water absorption of the three building materials

Figure 3 shows a comparison of the time evolution of the absorbed water mass at atmospheric and extremely low air pressures, as well as the average water content of the specimens. The completely saturated water content (open porosity) of the materials, as determined from the water content at vacuum saturation or mercury porosimetry, is also shown on the right-hand side.

While no evident changes were observed for the CS specimen at atmospheric and low pressures, the absorbed water mass at steady state increased at low air pressures for the brick and AAC specimens,

as shown by Janssen et al. (2015). Moreover, the results indicated that the absorption rates of the brick and AAC specimens increased at low air pressures. The absorption coefficient of the brick became 1.7 times larger at low air pressure. Notably, water absorption as a function of the square root of time appeared linear, even when the surrounding pressure was reduced. Furthermore, while the water content of the CS was close to the porosity after capillary absorption, even at atmospheric pressure, the water content of the brick and AAC was not. The brick specimens reached near-complete saturation only at a low air pressure. These results indicated the significance of the effects of air entrapment on water absorption.

It is worth noting that the gradient of the water absorption by AAC against the square root of the time elapsed from the start of water uptake decreased with time, while the brick and CS specimens clearly exhibit a linear relationship between the cumulative water absorption and the square root of elapsed time. It is known that some porous building materials, including AAC, exhibit such non-linear relationships (Hall 2007; Feng and Janssen 2018). Furthermore, the water absorption kinetics of AAC at a low air pressure exhibited different characteristics from those of brick and CS, which show linear relationships at both atmospheric and low air pressures. The absorbed water mass by AAC increased significantly at an early elapsed time compared with that at atmospheric pressure; however, the absorption rate was not large in the late stages of water absorption. As air entrapment is considered as a possible reason for the non-linear water absorption by some types of materials, including AAC, the water absorption characteristic at low air pressures should be further examined.

[insert Figure 3]

2.2.2 Water content profile during water uptake

Figure 4 shows a comparison of the water content profiles at atmospheric and extremely low air pressures. The results at the four representative measurement points are shown. Note that the air pressure in the desiccator when using a vacuum pump was approximately 7 kPa, which was slightly higher than that in the previous subsection because of the limitations of the experimental apparatus. Based on the figure, the differences between the two pressure conditions are clear; the material reached a higher water content at low air pressures than at atmospheric pressure. Furthermore, the water content increase started at an earlier elapsed time at a low air pressure. The water content at low pressure in the steady state was lower than the average water content observed in the previous experiment (Fig. 3 (a)), probably because of the relatively high air pressure in this experiment.

Figure 5 shows the water content profiles under the two pressure conditions as a function of the Boltzmann variable, which is expressed as $x / t^{0.5}$, where x is the distance from the water absorption surface (m) and t is time (s). The results at positions 20–80 mm from the water uptake surface are shown. Considering that gamma-ray measurements could not be conducted accurately near the

material surfaces because of the width of the emitted gamma rays (Fukui, et al., 2018), the results at the positions near the surfaces were excluded. The figure clearly shows that the material can reach a higher water content at a low air pressure, and the increase in water content starts at a large Boltzmann variable, that is, a short elapsed time. Notably, Fig. 5 demonstrates that the Boltzmann transformation is also valid when the surrounding air pressure is reduced (although this is natural based on the fact that the Boltzmann transformation follows the one-dimensional diffusion theory for one-component flow (Hall, 1977; Carmeliet, et al., 2004)). Therefore, despite the quantitative differences in the final water content and absorption rate, the nature of water uptake at ordinary and extremely low air pressures is the same.

[insert Figure 4]

[insert Figure 5]

2.3. Relationship between the pore structure of a material and air entrapment effects

To discuss the differences observed in the water uptake tests between the materials, we compared the experimental results with the pore structures of the materials. Based on the Young–Laplace equation and Boyle's law, Fagerlund (1994) proposed the following equation to predict the extent of air compression in a spherical pore owing to water uptake:

$$\alpha^{1/3}\left(\alpha^{-1}-1\right)=\frac{2\gamma}{p_0 r}, \tag{4}$$

where p_0 is the air pressure before compression (Pa), r is the pore radius (m), γ is the surface tension (N/m^2), and α is the ratio of the compressed air volume V/V_0. V_0 and V are the air volumes before and after compression, respectively. This equation indicates that the degree of air compression in a pore depends on its radius or capillary force. In finer pores, a large capillary force compresses the entrapped air more significantly.

Using this equation, we determined the ratio of compression α at both atmospheric and low air pressures, as listed in Table 1. These values correspond to the peak radius of the pore volume distribution (Fig. 1). For AAC, which exhibited two peaks, the peak at the larger pore radius was selected because it was expected that little air would remain at the peak with a smaller pore radius after water uptake, owing to the high capillary force (Fagerlund, 1994). CS has smaller pores than the other materials; therefore, the capillary force in the pores was larger and the absorbed water significantly compressed the air, even when water uptake occurred at atmospheric pressure. Consequently, the remaining air volume was predicted to be 7%. Fagerlund (1994) showed that the effects of air compression in such small pores on water uptake should be small because the compressed air volume is small and air dissolution is accelerated owing to the high pressure. Conversely, there are

large differences in α at atmospheric and low air pressures for brick and AAC, which explain the different water-absorption characteristics at different air pressures (Fig. 2). For the brick, α at a low air pressure was negligibly small, which explains the high water content (near complete saturation) after water uptake (Fig. 2 (a)). AAC has relatively large pores, so the air is not completely compressed even at low pressures. Therefore, some air remained in the pores during the water absorption tests at low air pressure.

Table 1. Peak pore radius and the ratio of the compressed air volume α related to the air volume before compression due to water uptake.

		Brick	CS	AAC
Peak pore radius (μm)		4.27	0.256	71.8
α	Under atmospheric pressure	0.72	0.07	0.98
	Under extremely low pressure (2 kPa)	0.01	0.00	0.40

It is worth noting that the predicted value of α for the brick at atmospheric pressure is considerably high considering the degree of liquid water saturation (w_l divided by the porosity) was 0.76 after capillary absorption, which means only 24% of the pore volume was occupied by air. Therefore, a considerable amount of air is expected to escape from the material during water absorption through the connection of pore spaces. The discussion presented here is under the assumption that air in a spherical pore is independently compressed due to water absorption. In the future, the significance of pore connectivity should be examined in more detail (e.g., based on pore network approaches (Descamps, 1997; Islahuddin and Janssen, 2019)).

3. Simultaneous air and water transfer simulations

3.1. Methods

3.1.1. Fundamental equations

We performed calculations corresponding to the water uptake of the bricks, as the difference in the water absorption at atmospheric and extremely low pressures is clear for the bricks, as presented in Figure 2 and Table 1. The mass-conservation equations for air and liquid water in a porous material (Fukui, et al., 2018; Green, et al., 1970) are as follows:

$$\frac{\partial w_a}{\partial t} = \frac{\partial}{\partial z}\left\{ k_a \left(\frac{\partial p_a}{\partial z} - \rho_a g \right) \right\}, \quad (5)$$

$$\frac{\partial w_l}{\partial t} = \frac{\partial}{\partial z}\left\{ \lambda'_P \left(\frac{\partial p_l}{\partial z} - \rho_l g \right) \right\}, \quad (6)$$

where g is the gravitational acceleration (m/s^2); k_a is the air conductivity (kg/(m·s·Pa)); p is the pressure (Pa); z is the position (m); and λ'_p is the water conductivity owing to the water pressure gradient (kg/(m·s·Pa)). The subscripts a and l denote air and liquid water, respectively. The water content (mass by volume) w is equal to $\rho\psi$, where ψ is the volume fraction (m^3/m^3). The sum of ψ_l and ψ_a is equal to the material porosity, and the air pressure is calculated based on the ideal gas law.

$$p_a \rho_a^{-1} = R_d T, \quad (7)$$

where R_d is the gas constant (J/(kg·K)) and T is the temperature (K).

3.1.2. Calculation conditions

The calculations were conducted one-dimensionally along the specimen height, that is, along the water uptake direction. Equations (5) and (6) were discretized using the finite-difference method. The discretization for time and space was conducted using forward and central differences, respectively, and the time and space steps were 1 mm and 5×10^{-6} s, respectively. The initial conditions for humidity in the material were set to 28%, which was the average humidity in the laboratory during the water uptake test at atmospheric pressure. The initial air pressure in the material was the atmospheric pressure (10^5 Pa). On the water absorption surface, the capillary pressure was set to −0.1 kPa and no air flow was considered. Values slightly below 0 kPa were used for the capillary pressure to avoid calculation errors. The air pressure on the surface exposed to air was set to atmospheric pressure. Vapor transfer was considered using the Robin boundary condition with an air humidity of 28% and the vapor transfer coefficient between the material surface and air was set to 4.16×10^{-8} (kg/(m^2·s·Pa)). The calculation was conducted under isothermal conditions and the material and air temperature was set to 23 °C.

3.1.3. Calculation cases

We performed the calculations as listed in Table 2. Calculations for Cases 1 and 2 were performed to validate the material properties and correspond to the water uptake tests at atmospheric and extremely low air pressures, respectively. Material properties are commonly measured at atmospheric pressure

and include implicit air entrapment effects, although these effects are ignored in most cases. Therefore, we used two sets of properties corresponding to atmospheric pressure and extremely low pressure for Cases 1 and 2, respectively. The calculation in Case 1 was based on an ordinary liquid water transfer calculation using the material properties corresponding to atmospheric pressure. Conversely, Case 3 was based on material properties, excluding the implicit air entrapment effects; however, it considered air transfer in the material instead, which also corresponded to water uptake at atmospheric pressure. Case 2, which corresponded to the water uptake tests at an extremely low air pressure, was also a water transfer calculation, as in Case 1, and the air transfer in the material was ignored because air compression was expected to be significant, as listed in Table 1.

Table 2. Calculation conditions.

	Fundamental equations	Air pressure to which the material properties correspond	Reproduced water absorption experiment
Case 1	Liquid water transfer (Equation (6))	Atmospheric pressure	Experiment at atmospheric pressure
Case 2	Liquid water transfer (Equation (6))	Extremely low pressure	Experiment at extremely low pressure
Case 3	Air and liquid water transfer (Equations (5) and (6))	Extremely low pressure	Experiment at atmospheric pressure

3.2. Material properties at atmospheric and extremely low air pressures.

3.2.1. Discussion on moisture transfer and retention characteristics with and without air entrapment effects

Based on the comparison of the water content profiles at different pressures (Figs. 4 and 5), the water transfer characteristics were qualitatively similar; particularly, the water content can be expressed as a single-value function of the Boltzmann variable in both cases. Thus, one-dimensional diffusion theory can be applied to these two cases.

Pressure plate measurement results used to derive the water retention curve are often obtained using initially vacuum-saturated specimens. Therefore, air entrapment effects were not included in the results. In the literature, the desorption curves from complete and capillary saturation were found to be similar below a certain humidity (Feng & Janssen, 2021), whereas they were different near saturation. When the pressure of the entrapped air developed in the pore space, the equilibrium relationship between the air and liquid water changed; the capillary pressure was higher than when assuming that the air pressure was maintained at atmospheric pressure (Fukui, et al., 2018). For the

288 employed bricks, the air pressure increased by approximately 39 kPa when compressed until the
289 volume decreased to 72% (Table 1). Such a capillary pressure shift owing to pore air pressure build-
290 up as a material approaches capillary saturation can be a reasonable explanation for the differences in
291 the water retention curve from complete and capillary saturation in a high-water-content region.
292
293 **3.2.2. Material properties used in the calculations.**
294 For the calculations, a water retention curve, moisture diffusivity, and air conductivity were necessary.
295 The moisture diffusivity of the bricks was derived using the ruler method (Evangelides, et al., 2018),
296 as shown in Fig. 6. The detailed procedures used for this determination are described in Appendix A.
297 Note that the Boltzmann transformation results shown in Fig. 5 were not used to derive the moisture
298 diffusivity because the air pressure was relatively large in the experiment and the air entrapment effects
299 could not be completely neglected.
300
301 [insert Figure 6]
302
303 The water retention curve at an extremely low air pressure (neglecting air entrapment effects) was
304 determined based on the suction curve found in the literature (Kumaran, 1996) using the following
305 form:

306
$$w_l = \frac{c_1}{c_2 + \exp\left(\log_{10} p_c - c_3\right)} + \frac{c_4}{c_5 + \exp\left(c_6\left(\log_{10} p_c - c_7\right)\right)}, \tag{8}$$

307 where p_c is the capillary pressure (Pa) (= $P_a - P_l$) and c_1–c_7 are constants. The values were multiplied
308 such that the water content at saturation corresponded to that at complete saturation of the employed
309 material. The function at the atmospheric pressure was then created such that the water content differed
310 from that at low air pressure only near saturation, as shown in Fig. 7. For the atmospheric-pressure
311 case: $c_1 = 95.5$; $c_2 = 8.0$; $c_3 = 5.0$; $c_4 = 263$; $c_5 = 1.5$; $c_6 = 2.8$; and $c_7 = 5.1$. For the low-pressure case:
312 $c_1 = 93.7$; $c_2 = 8.0$; $c_3 = 5.0$; $c_4 = 258$; $c_5 = 1.1$; $c_6 = 2.3$; and $c_7 = 5.0$. Notably, the differences between
313 the two curves were similar to the measured results for the water retention curves from complete and
314 capillary saturation, as reported in the literature (Feng & Janssen, 2021).
315
316 [insert Figure 7]
317
318 Finally, the air conductivity is given as a function of water content, as shown in Figure 8, based on
319 the two sets of measured data (see Appendix C for the measurement procedure). The curve was created

such that the air conductivity at capillary saturation was zero, assuming that air transfer did not take place above capillary saturation, except for the dissolution and diffusion phenomena.

[insert Figure 8]

3.3. Results and discussion

Figure 9 shows a comparison between the calculated and measured water absorption rates, and Fig. 10 shows the calculated water content and air pressure in the material for Case 3. The calculation results for Case 1 reproduced the results of the water uptake tests at atmospheric pressure. The results for Case 2 showed that the water diffusivity obtained from the water uptake tests at extremely low air pressure reproduced the water absorption rate. A comparison between the calculation results for Cases 2 and 3 demonstrates the significance of the effects of air present in the pores; the calculated water absorption rates decreased and the water content after capillary absorption decreased for Case 3. The differences between the calculated results for Case 3 and the measured results at atmospheric pressure can be attributed to uncertainties in the material properties, particularly in the low-pressure case.

According to Fig. 10, the air pressure increase is much slower than the water content increase. As the air conductivity of a material is high when the water content is low (as shown in Fig. 8), compressed air may move toward the dry region, and the pressure does not significantly increase during the early water uptake stages. This could potentially explain why the water transfer in porous building materials can be regarded as a single-phase phenomenon in most cases. Figure 11 shows the Boltzmann transformation results based on the calculated water content evolution shown in Fig. 10(a). In general, the relationship between water content and the Boltzmann variable at different positions coincides with each other. Therefore, these results also support that the Boltzmann transformation is often applicable to water uptake processes at ordinal pressures (e.g., Carmeliet, et al., 2004, Fukui, et al. 2021) even though the processes are actually two-phase phenomena.

In contrast, after the water content reaches a certain level, a significant air pressure development is observed, as shown in Fig. 10(b). This increase in air pressure prevents further water content increase. Subsequently, water transfer in a material is also limited as the water permeability of a material has a positive correlation with the water content. Consequently, both the saturated water content and absorption rates decreased at the atmospheric pressure compared with the low-humidity cases.

[insert Figure 9]

[insert Figure 10]

[insert Figure 11]

4. Conclusion

To understand the liquid water transfer characteristics of porous building materials in high-water-content regions, the effects of air entrapment must be understood under common water uptake conditions. Therefore, in this study, the water transfer characteristics at extremely low air pressures were examined via experiments and simulations. The experiments revealed that low air pressure increased the water absorption rates and water content after capillary absorption of the brick and autoclaved aerated concrete specimens, whereas the water uptake by the calcium silicate board specimens was not significantly affected. The differences among the materials can be attributed to the differences in the extent of air compression in the pores, which depends on the pore structure of the material based on Boyle's law.

The measurement of the water content profile using the gamma-ray attenuation method revealed that the water transfer characteristics are qualitatively similar at low and atmospheric air pressures, and one-dimensional water diffusion theory can be applied to water absorption in both cases, at least by materials following Darcy's law at ordinary pressure, such as bricks. To some extent, the simultaneous water and air transfer calculations reproduced the water uptake tests at atmospheric pressure. Therefore, the effects of air entrapment on the water behavior in a material can be explained based on Darcy's and Boyle's laws and the transfer and retention characteristics discussed in this paper.

The results of this study will help us understand the pure characteristics of water transfer without air entrapment effects and the interaction between air and liquid water in pores. Furthermore, the calculated water content and air pressure evolution indicated that air in pores moved toward the dry region when local water content was not high. Therefore, the pressure does not significantly increase despite significant air pressure development potentially occurring, which affects water transfer after the water content reaches a certain level. This supports the general assumption in the building physics field that treating the liquid water transfer in a material, such as bricks, as a one-component flow is valid in most cases. Therefore, currently, considering the air behavior in a material does not always seem necessary in hygrothermal simulations or material property determination. However, the findings of this study should be further expanded to understand the hygrothermal behavior in high-water-content regions close to and above capillary saturation and achieve more reliable hygrothermal property measurements.

Appendix A. Influence of the humidity conditions in a closed desiccator on water absorption

To assess the humidity conditions in the desiccator used for the water absorption tests at low air pressure and its influence on the water absorption by the specimens, we conducted an additional water absorption test in a closed desiccator. The measurement procedures were same as those for the water uptake tests described in Section 2.2.2; however, the pressure in the desiccator was maintained at the atmospheric pressure. During water absorption, humidity in the desiccator was also recorded.

391 The measurement results are shown in Fig. A1. In Fig. A1(b), additional measurement results for
392 the absorbed water mass at atmospheric pressure in the closed desiccator are compared with the other
393 results shown in Fig. 3(b). It is obvious that the humidity in the desiccator increased after it was closed,
394 and water absorption started (at 0 s) because of evaporation from the water reservoir and the high air
395 tightness of the desiccator. However, Fig. A1(b) shows that the results at atmospheric pressure (in the
396 laboratory) and in the closed desiccator were almost the same at an early elapsed time (see the results
397 at approximately 150 min (93 $s^{0.5}$)), and the influence of the humidity increase in the desiccator on the
398 water absorption was not significant. At a later elapsed time, the water absorption by the specimen in
399 the closed desiccator was larger than that measured in the laboratory because the specimen absorbed
400 vapor in the desiccator at the same time as water uptake from the reservoir. Based on these results, the
401 humidity conditions in the desiccator influenced the test results at a later elapsed time to some extent,
402 but the impact was not significant on most results presented in this paper as they were measured at a
403 relatively early elapsed time (several hours).
404
405 [insert Figure A1]
406
407 **Appendix B. Moisture diffusivity estimation at atmospheric and extremely low air pressures**
408 In the ruler method (Evangelides et al., 2018), the moisture diffusivity is derived without using the
409 water content distribution evolution in a material during water uptake. Instead, the Boltzmann variable
410 λ_f (m/$s^{0.5}$) at the wetting front was determined from visual observations. Using λ_f, parameters a, b, and
411 c in the following approximate curve for the water content as a function of the Boltzmann variable are
412 estimated:

413 $$w_l(\lambda) = -\left[a \tan^{-1}(b\lambda + c)\right]. \quad \text{(B1)}$$

414 The parameters were determined with the two boundary conditions, that is, $w_l = 0$ at $\lambda = \lambda_f$ and $w_l =$
415 w_{sat} at $\lambda = 0$, where w_{sat} is the saturated water content (kg/m^3), and the following relationship regarding
416 absorption coefficient A (kg/($m^2 \cdot s^{0.5}$)):

417 $$A = \int_0^{w_{cap}} \lambda dw. \quad \text{(B2)}$$

418 Using Eq. (B1) with the determined values of a, b, and c, the moisture diffusivity D_w (m/s) is derived
419 from the following equation (Carmeliet et al., 2004):

$$D_w(w) = -\frac{1}{2}\frac{\int_{w_0}^{w_l} \lambda dw_l}{\partial w_l / \partial \lambda} \quad . \tag{B3}$$

Table B1 lists all the necessary parameters to determine D_w using Eqs. (B1)–(B3). To determine λ_f at atmospheric pressure, an additional water uptake test including visual observations was conducted. It is difficult to measure λ_f at low pressure (in the vacuum desiccator). To apply the value of the low-pressure case, we first determined the time t_{sat} (s) required for the specimen to reach saturation. The values were determined to be 88^2 and 110^2 s at atmospheric and low air pressures, respectively, based on the time evolution of the absorbed water mass, as shown in Fig. B1. Then, we assumed that the wetting front movement rate was inversely proportional to t_{sat}. This assumption allowed us to determine λ_f at a low air pressure, which was found to be 0.00149, based on λ_f at atmospheric pressure and t_{sat} (= 0.00120 × (88 / 110)). In addition, A was derived from the water uptake tests, and w_{sat} was set to the water content at the capillary and complete saturation states for deriving D_w at atmospheric and extremely low pressures, respectively.

[insert Figure B1]

Table B1 Parameters used to estimate the moisture diffusivity at atmospheric and extremely low air pressures

		Atmospheric pressure	Low pressure
Water absorption coefficient A (kg/(m^2·s$^{0.5}$))		0.181	0.278
Saturated water content w_{sat} (kg/m^3)		187	246
Boltzmann variable at the wetting front λ_f (m/s$^{0.5}$)		0.00120	0.00149
Parameters in Eq. (A1)	a	253	344
	b	8.25 × 10^3	4.16 × 10^3
	c	-10.8	-7.1

Appendix C. Air conductivity measurement

The air conductivity was determined based on the Cembureau method specified in the RIREM recommendation (RILEM Technical Committees, 1999). A 50-mm-thick brick specimen with a 83-mm diameter was placed in a permeameter cell, and the flow rate Q (m^3/s) of N_2 gas through the

specimen was measured (see Fig. 2 in RILEM Technical Committees (1999). Based on the measured values of Q, the air conductivity was determined as follows:

$$k_a = \frac{2P_{atm}\rho_a QL}{A\left(P_i - P_{atm}\right)}, \tag{9}$$

where A is the cross-sectional area of the specimen (m^2), L is the specimen thickness (m), and P_i and P_{atm} are the applied and atmospheric pressures (Pa), respectively.

The measurements were conducted using a specimen in air-dry and wet (after 6 h of water immersion) states. The RIREM recommendation specifies to start the test from an applied pressure of 150 kPa. However, applying this pressure on the brick specimen caused a large flow rate; therefore, a lower pressure was applied. The test conditions and results are listed in Table C1.

Table C1 Conditions and measured flow rates in the tests using the Cembureau method

Sample condition	Applied pressure	Flow rate
Air-dry	5 kPa	3.3×10^{-6} m^3/s
Wet	25 kPa	4.3×10^{-6} m^3/s

References

Carmeliet, J. et al., 2004. Determination of the liquid water diffusivity from transient moisture transfer experiments. *Journal of Thermal Envelope and Building Science,* Volume 27, pp. 277-305.

Descamps, F., 1997. *Continuum and discrete modelling of isothermal water and air flow in porous media.* Leuven: Dissertation, KU Leuven.

Evangelides, C. et al., 2018. Moisture estimation in building materials with a simple procedure. *Construction and Building Materials,* 164(2018), pp. 830-36.

Fagerlund, G., 1977. The critical degree of saturation method of assessing the freeze/thaw resistance of concrete. *Matériaux et Construction,* Volume 10, pp. 217-29.

Fagerlund, G., 1994. *Predicting the service life of concrete exposed to frost action through a modelling of the water absorption process in the air-pore system (Report TVBM (Intern 7000-rapport); Vol. 7085).* Lund: Division of Building Materials, LTH, Lund University..

Feng, C. et al., 2020. Hygric properties of porous building materials (VI): A round robin campaign. *Building and Environment,* Volume 185, p. 107242.

Feng, C. & Janssen, H., 2018. Hygric properties of porous building materials (III): Impact factors and data processing methods of the capillary absorption test. *Building and Environment,* Volume 134, p. 21-32.

Feng, C. & Janssen, H., 2021. Hygric properties of porous building materials (VII): Full-range benchmark characterizations of three materials. *Building and Environment,* Volume 15, p. 107727.

Feng, C., Janssen, H., Feng, Y. & Meng, Q., 2015. Hygric properties of porous building materials: Analysis of measurement repeatability and reproducibility. *Building and Environment,* Volume 85, pp. 160-72.

Feng, C., Roels, S. & Janssen, H., 2019. Towards a more representative assessment of frost damage to porous building materials. *Building and Environment,* Volume 164, p. 106343.

Fukui, K., Iba, C., Hokoi, S. & Ogura, D., 2018. Effect of air pressure on moisture transfer inside porous building materials. *Japan Architectural Review,* Volume 1, pp. 538-47.

Fukui, K. et al., 2022. Investigation into the hygrothermal behavior of fired clay materials during the freezing of supercooled water using experiments and numerical simulations. *Journal of Building Physics,* Volume 45, pp. 723-75.

Green, D. W., Dabiri, H., Weinaug, C. F. & Prill, R., 1970. Numerical modeling of unsaturated groundwater flow and comparison of the model to a field experiment. *Water Resources Research,* Volume 6, pp. 862-74.

Hall, C., 1977. Water movement in porous building materials—I. Unsaturated flow theory and its applications. *Building and Environment,* Volume 12, pp. 117-25.

Hall, C., 2007. Anomalous diffusion in unsaturated flow: Fact or fiction?. *Cement and Concrete Research,* Volume 37, pp. 378-85.

Iba, C. & Hokoi, S., 2009. Measurement of water permeability of roof tiles and influence of entrapped air. *Journal of ASTM International,* Volume 6, p. JAI102030.

Iba, C. et al., 2023. Deterioration mechanism and hygrothermal condition of tuff stones used for exteriors at former Koshien Hotel. *Journal of Cultural Heritage,* Volume 61, pp. 139-49.

Islahuddin, M. and Janssen, H., 2019. Pore-structure-based determination of unsaturated hygric properties of porous materials. *Transport in Porous Media,* Volume 130, pp. 675-98.

Janssen, H., Vereecken, E. & Holúbek, M., 2015. A confrontation of two concepts for the description of the overcapillary moisture range: air entrapment versus low capillarity. *Energy Procedia,* Volume 78, pp. 1490-94.

Kumaran, M. K., 1996. *IEA Annex 24, Final Report, Vol. 3, Task 3: Material Properties.* Leuven: Laboratorium Boufysica, Department Burgerlijke Bouwkunde, KU Leuven.

Künzel, H. M., 1995. *Simultaneous heat and moisture transport in building components: One- and two-dimensional calculation using simple parameters.* s.l.:Fraunhofer IRB Verlag Suttgart.

Nielsen, A. F., 1972. Gamma-ray-attenuation used for measuring the moisture content and homogeneity of porous concrete. *Building Science,* Volume 7, pp. 257-63.

RILEM Technical Committees, 1999. RILEM TC 116-PCD: Permeability of Concrete as a Criterion of its Durability. *Materials and Structures,* Volume 32, pp. 174-79.

508 Rirsch, E. & Zhang, Z., 2010. Rising damp in masonry walls and the importance of mortar properties.
509 *Construction and Building Materials,* Volume 24, pp. 1815-20.
510 Roels, S. et al., 2004. Interlaboratory Comparison of Hygric Properties of Porous Building Materials.
511 *Journal of Building Physics,* Volume 27, pp. 307-25.
512 Vachaud, G., Gaudet, J. P. & Kuraz, V., 1974. Air and water flow during ponded infiltration in a
513 vertical bounded column of soil. *Journal of Hydrology,* Volume 22, pp. 89-108.
514 Wang, Z., Feyen, J., van Genuchten, M. T. & Nielsen, D. R., 1998. Air entrapment effects on
515 infiltration rate and flow instability. *Water Resources Research,* Volume 34, pp. 213-22.
516 Zhou, M., Li, X., Feng, C. & Janssen, H., 2022. Hygric properties of porous building materials (VIII):
517 Influence of reduced air pressure. *Building and Environment,* Volume 225, p. 109680.
518

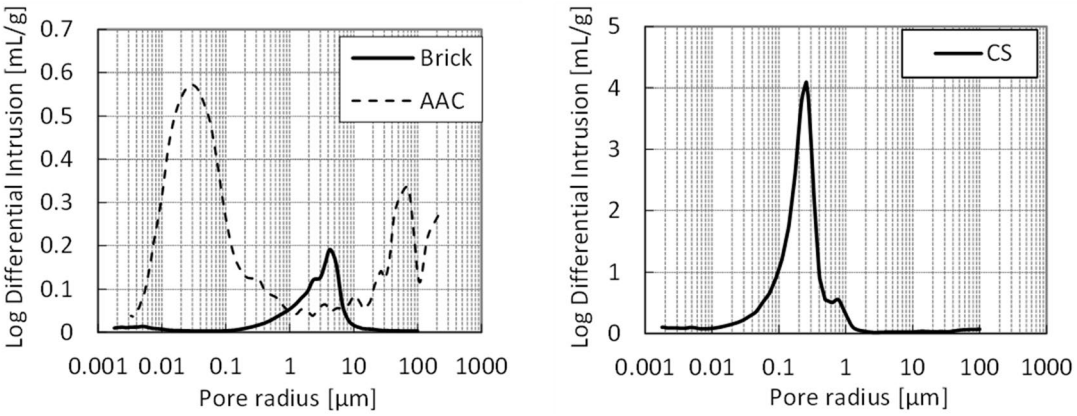

(a) (b)

Figure 1. Pore volume distribution of the employed three materials: (a) brick and autoclaved aerated concrete (AAC), and (b) calcium silicate board (CS).

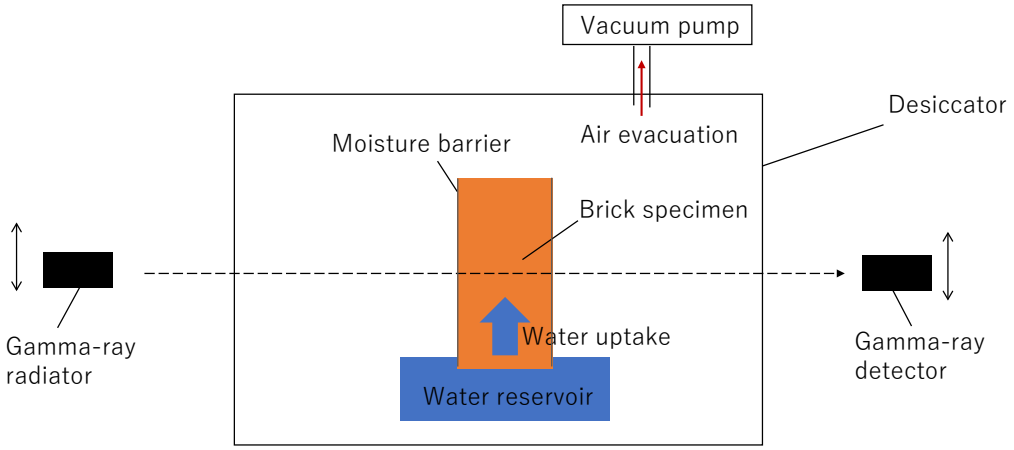

Figure 2. Experimental setup of water uptake test at the low air pressure using gamma-ray attenuation apparatus.

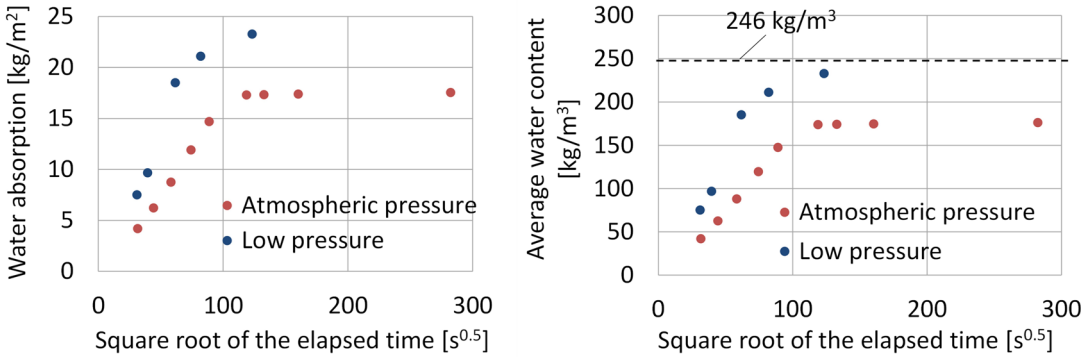

(a)

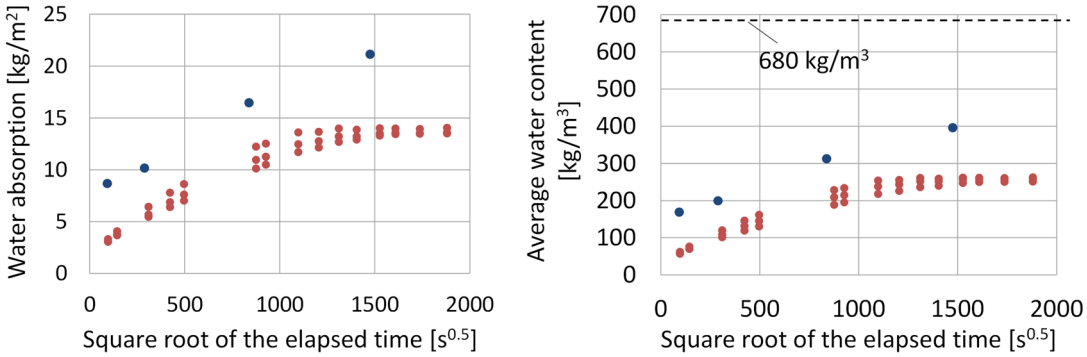

(b)

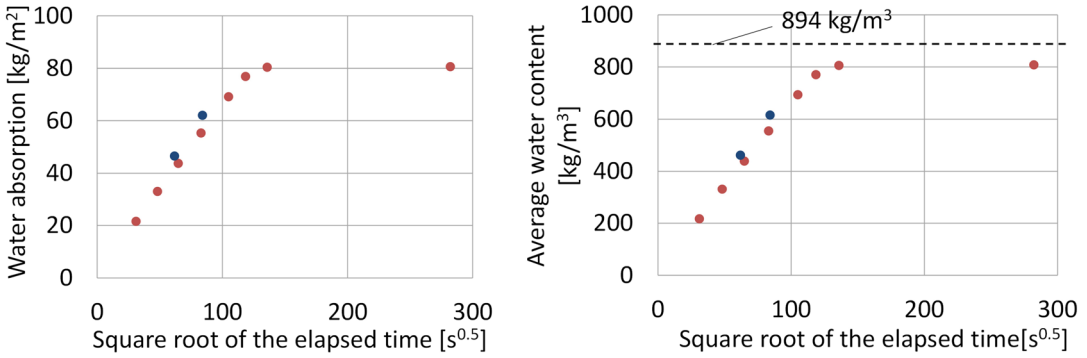

(c)

Figure 3. Time evolution of the mass of the absorbed water and average water content of the (a) brick, (b) autoclaved aerated concrete, and (c) calcium silicate board specimens at atmospheric and extremely low pressure.

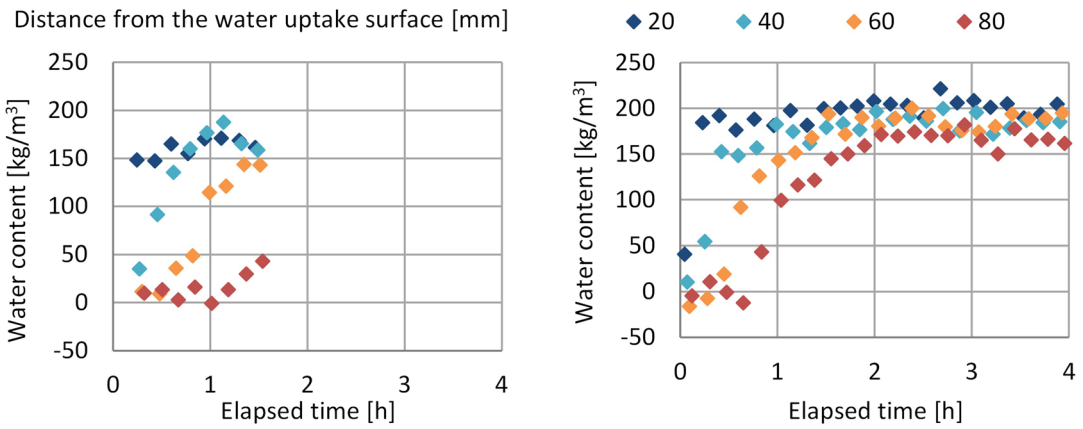

(a) (b)

Figure 4. Water content profile in the brick specimens during water uptake at (a) atmospheric and (b) extremely low (9 kPa) air pressures.

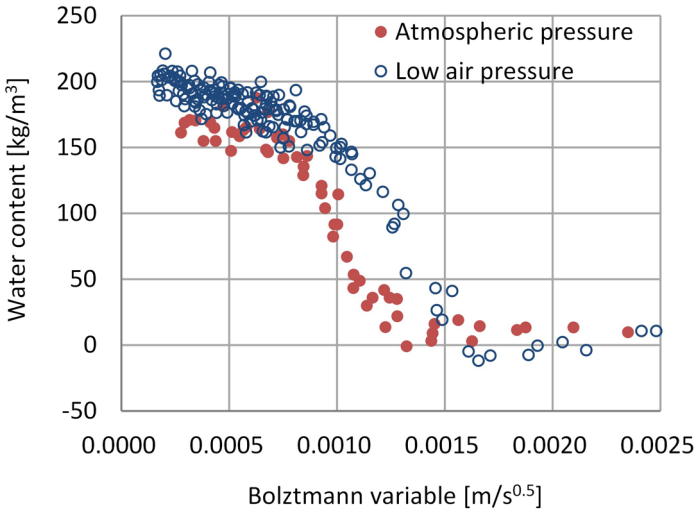

Figure 5. Comparison of the water content of the brick specimen during water uptake as a function of Boltzmann variable at atmospheric and extremely low (9 kPa) air pressures.

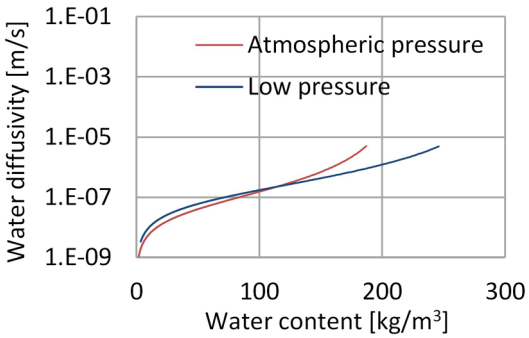

Figure 6. Water diffusivity for the atmospheric and extremely low air pressure.

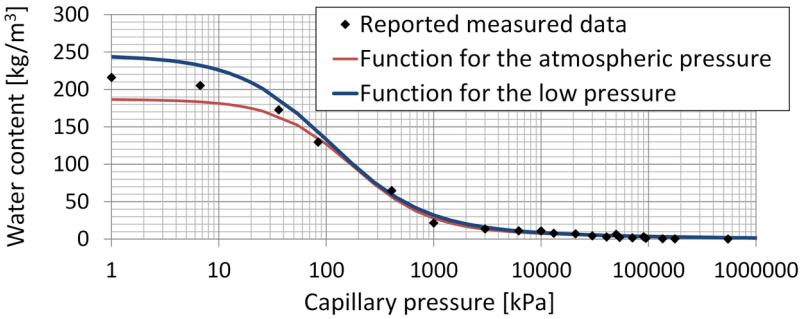

Figure 7. Water retention curve for the atmospheric and extremely low air pressure.

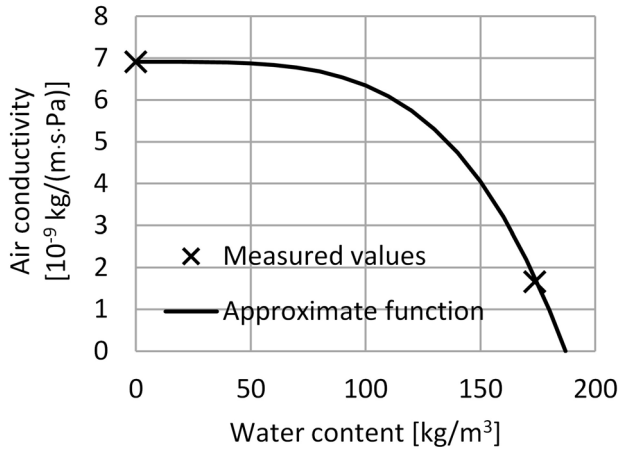

Figure 8. Air conductivity used in the calculation.

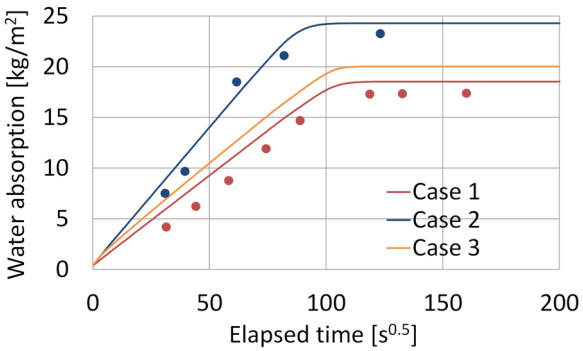

Figure 9. Comparison between the calculated (lines) and measured (markers) water absorption at the atmospheric and extremely low air pressure.

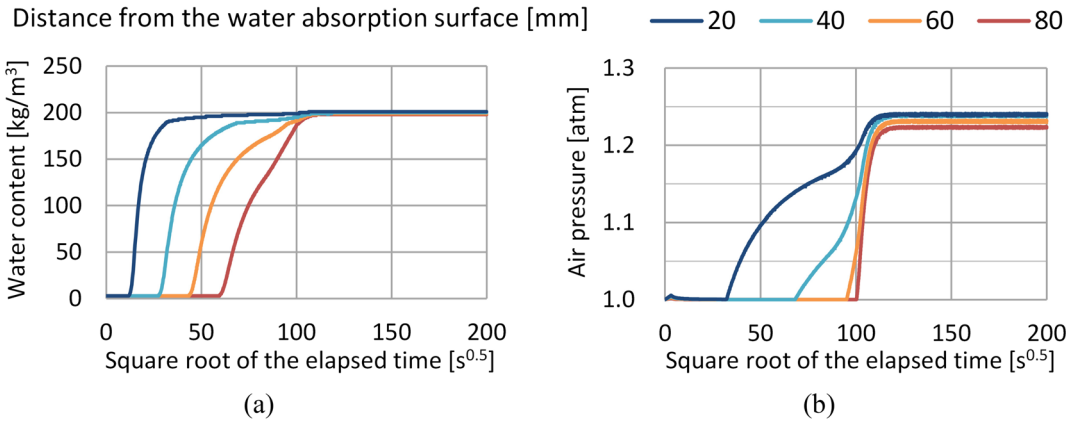

Figure 10. Calculated results of the (a) water content and (b) air pressure in the material.

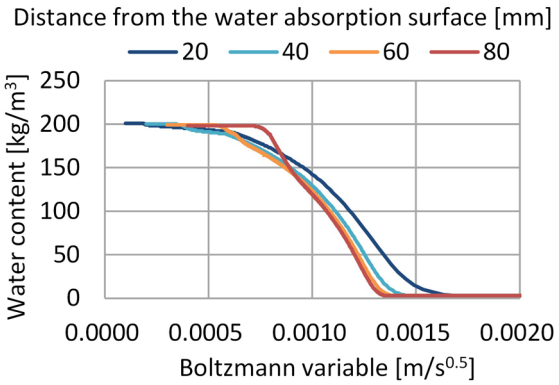

Figure 11. Calculated water content as a function of the Boltzmann variable.

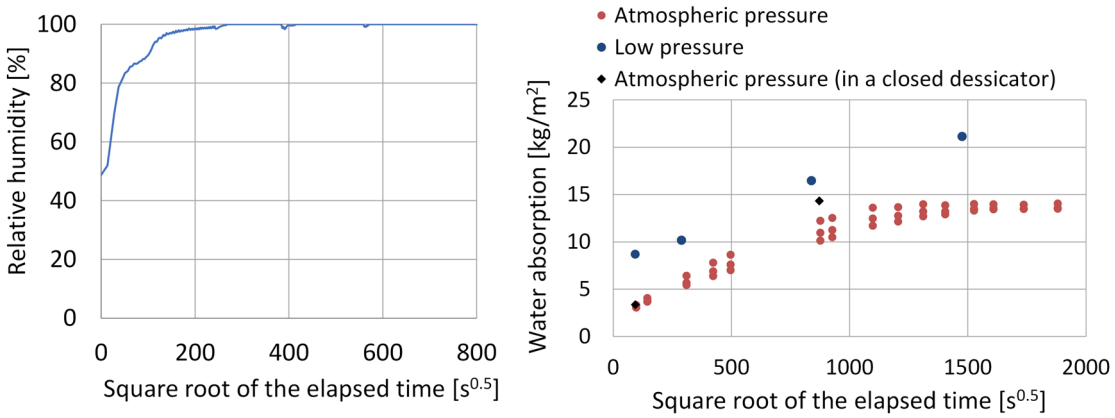

(a) (b)

Figure A1 (a) Time evolution of the humidity and (b) water absorption by aerated concrete in a closed desiccator.

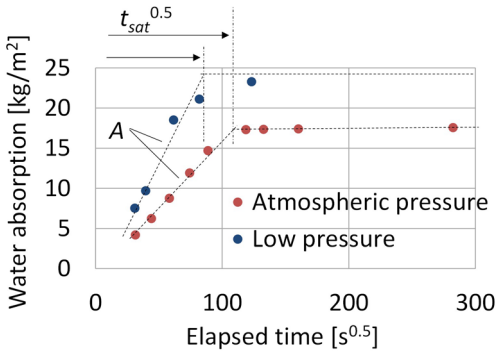

Figure B1 Comparison of the water absorption at the atmospheric and extremely low air pressure.